Article

# The Role of Surface Diffusion in the Growth Mechanism of Triosephosphate Isomerase Crystals

Mike Sleutel, Celine Vanhee, Cécile Van de Weerdt, Klaas Decanniere, Dominique Maes, Lode Wyns, and Ronnie Willaert

*Cryst. Growth Des.*, **2008**, 8 (4), 1173-1180 • DOI: 10.1021/cg0703691 • Publication Date (Web): 18 March 2008



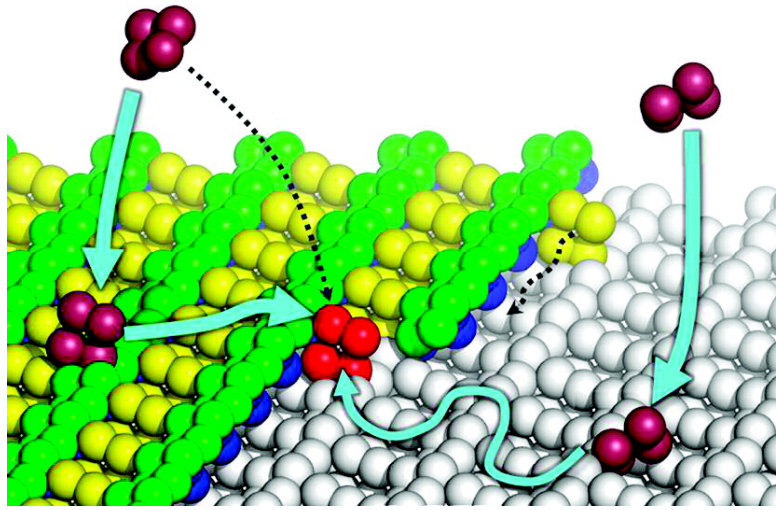

CRYSTAL GROWTH & DESIGN
2008
VOL. 8, NO. 4
1173–1180

# The Role of Surface Diffusion in the Growth Mechanism of Triosephosphate Isomerase Crystals

Mike Sleutel,*,† Celine Vanhee,† Cécile Van de Weerdt,‡ Klaas Decanniere,† Dominique Maes,† Lode Wyns,† and Ronnie Willaert†

*Ultrastructuur, Flanders Interuniversity Institute for Biotechnology, Vrije Universiteit Brussel, Belgium, and Labo de Biologie Moléculaire et de Génie Génétique, Université de Liège, Belgium*

*Received April 16, 2007; Revised Manuscript Received December 27, 2007*

**ABSTRACT:** In the protein crystallization process, a growth unit has two possible molecular pathways it can follow from solution to the crystal bulk, namely, the process of direct incorporation from solution or the process of surface diffusion preceded by surface adsorption. We use real time in situ atomic force microscopy to monitor the molecular processes that govern the crystallization of the protein triosephosphate isomerase. With this technique, we study the step edge dynamics on a molecular scale. We conclude that step reorganization as a result of line diffusion has a negligible effect on step dynamics. Therefore, step displacements are attributed to the exchange of growth units with the surrounding phases, i.e., the terrace and the solution. Triosephosphate isomerase (TIM) tetramers are identified to be the dominating growth units. From the statistics of molecular attachment and detachment from the step, we conclude that the incorporation of growth units occurs through surface diffusion. Additionally, in the tested supersaturation range, normal growth is dominated by the two-dimensional nucleation of triangular islands. The step edges of these islands have equal step formation energy.

## 1. Introduction

With an annual growth of more than 5000 protein X-ray structures, the protein databank[1] contains at present a total of 31.000 protein structures, from which only a mere ~0.8% are solved to subangstrom resolution. This fact stands in sharp contrast to the vastly increasing need to reveal atomic microstructures at 1 Å or less. Such a shortcoming is not surprising though, considering that obtaining high-resolution structures requires near perfect crystals. This need for perfection is due to the fact that biomacromolecular crystals can have lattice spacings reaching tens of nanometers. Because size, macroscopic formations, and most defects are under kinetic control, the acquisition of quasi flawless crystals requires a very good understanding of the growth mechanism and therefore the kinetics of the crystallization process.

On a mesoscopic length scale, crystal growth proceeds through two different processes, i.e., normal and tangential growth.[2] In the case of normal growth, new growth layers are generated through either two- or three-dimensional nucleation on the crystal surface or through the generation of spiral dislocations by the presence of lattice defects. Perpendicular to this growth mode is the mechanism of tangential growth, which is the horizontal spread of existing layers across the surface through the addition of new molecules in growth sites, named kinks.

The kinetics of these different growth regimes determines the crystal surface morphology, which in turn influences the X-ray diffraction characteristics of the crystal. For instance, it was shown that step bunching can have a detrimental effect on the diffraction quality and therefore the utility of the protein crystal.[3] To understand these mesoscopic events that determine crystal surface morphology and thus crystal quality, it is necessary to study and ultimately comprehend the underlying molecular-level mechanisms that govern their growth. Vital in this understanding is unravelling the molecular pathway a molecule will follow from solution to the crystal bulk.

In the specific case of tangential growth, two types of mass transfer pathways of the growth units toward the steps can be discerned, namely, the process of direct incorporation from solution and the process of surface diffusion preceded by surface adsorption.[4] Although the total change in the average energy of a particle as it moves from the solution to the interface is the same for both pathways, the energy activation barriers the particle has to overcome can differ for both trajectories. The relative heights of these barriers that need to be surmounted, will determine the dominating transport mechanism. The determination of the ruling solute pathway has proven to be quite difficult. Not surprisingly, the significance of surface diffusion remains a long-standing problem of fundamental interest.[5] For the case of crystallization of small molecules from solution, direct incorporation of calcite,[6] silver,[7] theophylline monohydrate,[8] ammonium dihydrogen phosphate (ADP),[9] and potassium dihydrogen phosphate (KDP)[9,10] has been observed. For those last two, however, Vekilov et al.[11] and DeYoreo et al.[12,13] have suggested the possibility that surface diffusion does contribute significantly to the surface kinetics.

In the case of biomacromolecular crystallization, mesoscale evidence that favors a multistage process involving adsorption on the surface and two-dimensional diffusion toward the steps has been presented for a few model proteins only, i.e., canavalin,[14] insulin,[15] and the (110) face of lysozyme.[16,17] In contrast, for the (010) face of orthorhombic lysozyme, it has been shown that surface diffusion has a negligible contribution to tangential growth.[18] One of the possible caveats of interpreting mesoscale data in favor of direct incorporation is that the prerequisite of interstep interaction, i.e., surface diffusion field overlap, is not met in the tested experimental conditions. This problem does not occur when studying step dynamics at a molecular level using atomic force microscopy (AFM), where interstep interactions are not required to identify ruling mass transfer mechanisms. This type of high-resolution experiments on protein crystals have only been performed by Chen et al.,[19]

* Corresponding author. Address: Ultrastructuur (ULTR), Vrije Universiteit Brussel, Oefenplein, Building E, Pleinlaan 2, 1050 Elsene, Belgium. E-mail: mike.sleutel@vub.ac.be. Tel: 32-2-6291923. Fax: 32-2-6291963.
† Vrije Universiteit Brussel.
‡ Université de Liège.

10.1021/cg0703691 CCC: $40.75 
Published on Web 03/18/2008

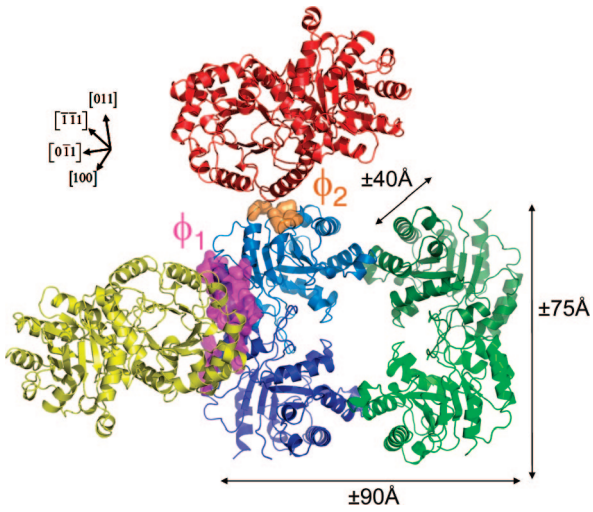


**Figure 1.** TIM tetramer (114 kDa), a dimer of dimers (blue and green). Two interconnecting symmetry related dimers are displayed in yellow and red. The two different types of lattice contact patches are shown: the strong interaction $\varphi_1$ (magenta) and the $\varphi_2$ (orange).

from which critical evidence was found for the surface diffusion mechanism in the crystallization of apoferritin and ferritin, a very large iron storage protein measuring 13 nm in size with a molecular mass of 550–950 kDa.[20] Ferritin, however, is a special case of protein crystallization because the electrolyte $Cd^{2+}$ does not only screen repulsive forces, it is also involved in specific bonds between the similarly charged molecules.[4]

In this paper, using AFM we determined the dominating mass transport system for the case of the crystallization of the noncommercially available protein triosephosphate isomerase (TIM) from the hyperthermophillic bacterium *Thermotoga maritima*. The enzyme is a tetramer, assembled as a dimer of dimers, with a total molecular mass of 114 kDa (Figure 1). The crystal structure has been solved and refined at 2.85 Å resolution in a primitive trigonal form.[21] The electrolyte that was used for the crystallization is ammonium sulfate. Having a usage rate of 30% in the Biological Macromolecule Crystallization Database,[22] ammonium sulfate is a very common and successful precipitant and is not involved in any specific bonds for the case of TIM.

## 2. Experimental Section

**2.1. Protein Crystallization.** Triosephosphate isomerase from *Thermotoga maritima* (TIM) was produced and purified as described previously.[21] Crystals were grown at 20 °C using the sitting drop vapor diffusion technique with the aid of microbridges (Hampton Research, California) and nonsiliconised 10 mm diameter glass discs. The protein solution used in the crystallization set-ups contained 20 mg/mL protein in 100 mM Tris-HCl pH 8.0 and 200 mM NaCl. Drops were prepared by mixing 2 $\mu$L of TIM solution with 2 $\mu$L reservoir solution of 100 mM Tris-HCl pH 8.0, 200 mM NaCl, and 2.0 M ammonium sulfate. Twenty-four to 48 h later, the crystal size varied between 50 and 500 $\mu$m with some crystals adhering to the glass discs. From the nonadhering crystals, the space group was determined to be $P3_221$ using X-ray diffraction. Adhering crystals with surfaces parallel to the scanning plane were selected for the AFM measurements.

**2.2. Atomic Force Microscopy.** The glass discs containing the adsorbed crystals were glued to metal pucks with two component epoxy glue and were placed onto the AFM scanner. Approximately 50 $\mu$L of growth solution was added to the sample, the O-ring was installed to prevent evaporation, and the fluid cell was mounted into the scanner head. The system was stabilized for 60 min to avoid drift of the set point. AFM imaging of the crystallization processes was conducted in tapping mode using Nanoscope IIIa multimode AFM (Veeco, Santa Barabara, CA). Tip resonance frequencies were readjusted when the tip was lowered to within 30 $\mu$m of the sample surface. Images were acquired in buffer solutions of identical composition to the mother liquor, but at varying TIM and ammonium sulfate concentrations. In situ temperature measurements in the fluid cell revealed a temperature of 28–29 °C while scanning. Standard silicon nitride and oxide sharpened Nanoprobe SPM tips (Veeco, Santa Barabara, CA) were used. Cantilevers with nominal force constants of 0.01 N/m were typically utilized. The tapping drive frequency was adjusted in the range 8–10 kHz to the resonance value of the employed tips. To minimize the force applied to the crystalline surface during scanning, we continually adjusted the set point voltage to the lowest level for which tip-crystal contact was maintained.

**2.3. High-Resolution AFM Imaging and X-ray Data Modeling.** High resolution images from areas on the terraces between the steps of the habit-forming faces were acquired in tapping mode without O-ring. Fourier filtering was performed using the Groningen Image Processing software package (http://bfcemw0.chem.rug.nl/progs-grip.html) on a Linux workstation. Crystal lattice parameters were measured using the Nanoscope software v5.12 (Veeco, Santa Barbara, CA). In silico models of various Miller planes (hkl) were generated by applying a set of standard $P3_221$ symmetry operators on the TIM structure (pdb-code 1B9B). The hereby obtained pdb-files were loaded into Pymol (http://www.pymol.org) to generate graphical representations of the crystal planes. Residues participating in lattice contacts were identified using the Protein–Protein Interaction Server (http://www.biochem.ucl.ac.uk/bsm/PP/server/index.html) and were grouped in lattice contact $\varphi_1$ and $\varphi_2$ (Figure 1).

**2.4. Wulff Construction.** To calculate the relative values of the step formation energy per unit length ($\beta$), we used the expression of Khare[23] in polar coordinates $(R,\theta)$ for two-dimensional equilibrium islands

$$\beta(\varphi) = \lambda \frac{R(\theta)}{\left(1 + \left(\frac{\partial R(\theta)}{\partial \theta} \Big/ R(\theta)\right)^2\right)^{1/2}} \quad (1)$$

with $\varphi = \theta - \arctan(\partial R(\theta)/\partial\theta)$, $R(\theta)$ the distance between the center of mass of the island and the step edge at a given angle $\theta$ and the proportionality constant $\lambda$ being the equilibrium island chemical potential per unit area. Because relative values of $\beta$ suffice for our purposes, $\lambda$ was set to unity.

## 3. Results and Discussion

**3.1. Crystal Face Identification.** The obtained TIM crystals exhibit a highly faceted crystal habit. Consequently, direct macroscopic identification (of the Miller indices) of the crystal faces that make up the crystal habit is an error prone process. To facilitate the identification of the crystal face that was studied in the AFM experiments, high-resolution AFM images of areas on the terraces between the steps of the habit-forming faces were recorded (Figure 2). After Fourier filtering, the crystal lattice parameters (i.e., intermolecular distances and angles) were measured (Figure 3): 168/164/130 Å and 68/44°. Next, using the X-ray structure of TIM,[21] we constructed a multitude of Miller planes in different crystallographic directions in silico. From these models the intermolecular distances and angles were determined (163.1/163.1/126.0 Å and 67.3/45.4°). On the basis of the highest similarity between lattice parameters derived from AFM and X-ray structural data for various directions, the crystal face was identified to be the (011) plane. However, the molecules comprising the (011) Miller plane do not make up an entire growth layer on the crystal face (not shown). From the created models, it became clear that a single growth layer can be generated using two stacked parallel (011) Miller planes. The tetramers belonging to the top plane appear in the crevices between the molecular rows from the underlying plane (Figure 4a). Therefore, a single growth layer is comprised of the yellow and green tetramers from a single (011) Miller plane and of the blue tetramers coming from a parallel (011) Miller plane stacked above it. Additionally, on the basis of X-ray data, the height of

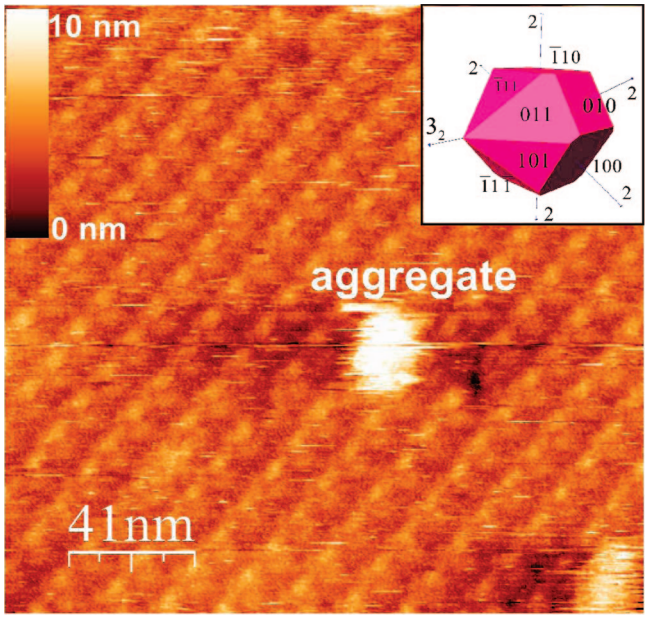


**Figure 2.** High-resolution unfiltered AFM height image obtained in tapping mode. In the center of the image, a TIM aggregate is adhered onto the surface. Individual TIM tetramers are clearly visible; top left inset, height scale; top right inset, trigonal TIM crystal.

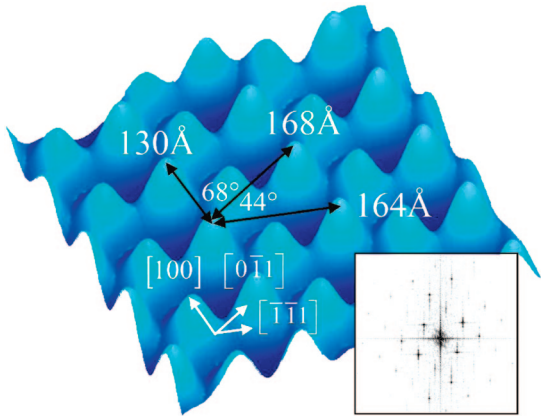


**Figure 3.** Fourier filtered image of a high-resolution height image (Figure 2) from which intermolecular distances and angels of the crystal lattice were obtained; inset: Fourier transform of Figure 2.

a step edge was determined to be ±65 Å (Figure 4b). This agrees very well with the experimentally determined step height from the AFM images 62 ± 3 Å, corresponding to the height of a slightly depressed single tetramer. Note that the blue tetramer is depressed with respect to the green and yellow tetramer, resulting in molecular bands across the surface in the [1̄1̄1] direction. These bands correspond to the horizontal molecular rows in Figure 3.

**3.2. Crystal Growth on the (011) TIM Face. 3.2.1. Normal Growth through Two-Dimensional Nucleation.** For the case of TIM, we observed that normal growth on the (011) face is dominated by the formation of two-dimensional islands. This is true for most studied macromolecular crystals, especially at higher supersaturations.[24–27] In the tested supersaturation range of $\sigma = \ln(C/C_e) = 1.6-5.8$ with $C$ the used protein concentration and $C_e$ the equilibrium protein concentration, no spiral dislocations have been observed. To fully exclude this growth mechanism for TIM, we need to perform additional experiments at conditions closer to equilibrium.

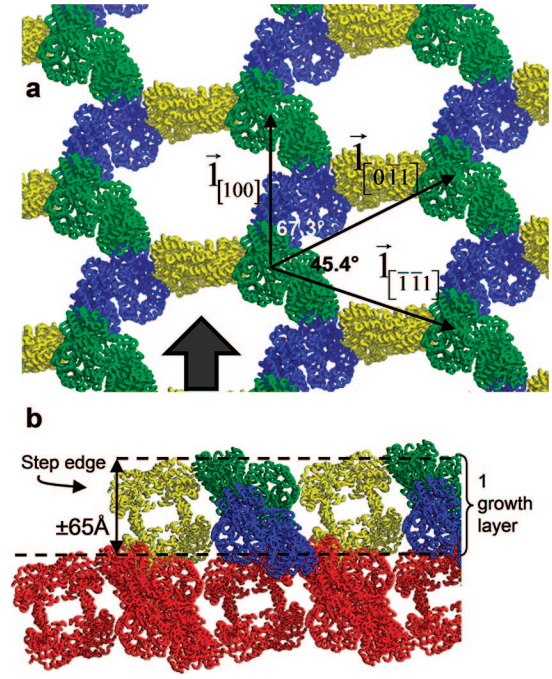


**Figure 4.** (a) In silico model of (011) growth layer perpendicular to the 3-fold screw axis with intermolecular distances and angles depicted: $|\vec{1}_{[100]}| = 126.0$, $|\vec{1}_{[01\bar{1}]}| = 163.1$, and $|\vec{1}_{[\bar{1}11]}| = 163.1$ Å. Tetramers belonging to the underlying growth layer (red tetramers) have been omitted. (b) Side view of a step edge on a (011) crystal plane (direction indicated by block arrow in (a)); step height is estimated to be ±65 Å.

The observed 2D islands have a triangular shape, which indicates an anisotropy in the rates of step advancement along different crystallographic directions. Such striking asymmetric islands have been reported for thaumatin and beef liver catalase.[24] This growth asymmetry most likely translates back from the asymmetry of the growth unit itself, whether it is a single molecule, an oligomer, or a complete unit cell. Although all molecules in the crystal bulk experience the same crystallographic interactions, molecules on the surface sense different physicochemical environments. The set of molecular interactions a surface molecule will feel and the different portions of their surface it will bury, depend greatly on the asymmetric unit position a molecule occupies.[28] Anisotropic shaped 2D islands may therefore arise from restricted mobilities along the edges[29] or differences in activation barriers for attachment and detachment from the step.

Molecular resolution imaging of the 2D islands shows that the step edges of the islands are aligned with the intermolecular vectors of the crystal lattice (Figure 5). Moreover, for the sampled supersaturation range the ratio of the step edge lengths $\vec{s}_{[100]}/\vec{s}_{[01\bar{1}]}/\vec{s}_{[\bar{1}11]}$ of the islands is 1/1.3 ± 0.2/1.3 ± 0.2. Additionally, the ratio $\vec{1}_{[100]}/\vec{1}_{[01\bar{1}]}/\vec{1}_{[\bar{1}11]}$ of the intermolecular vectors based on X-ray data is 1/1.3/1.3. Therefore, the same number of unit cells is incorporated in the three different island edges as a function of time.

This anisotropic equilibrium island shape can be related to a fundamental crystal parameter, the step edge free energy $\beta(\varphi)$[30,31]. $\beta(\varphi)$, the two-dimensional (2D) analog of the surface free energy, will determine the equilibrium island shape (EIS) of the 2D islands. Assuming that the islands have equilibrium shapes, we can estimate the angular dependence of the relative values $\beta(\varphi)$ by using the analytical expressions of the Wulff theorem in generalized polar coordinates.[23] To correct for the

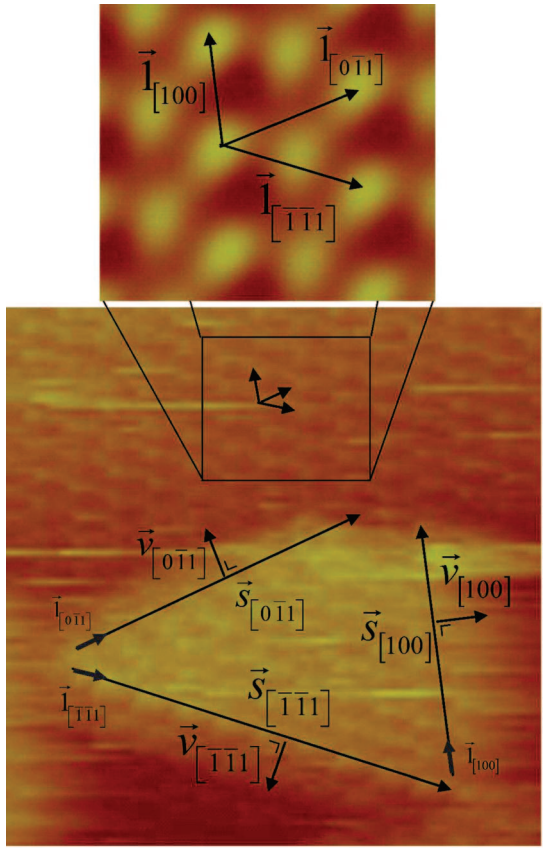


**Figure 5.** Top: Fourier filtered zoom-in of (011) crystal face, with intermolecular vectors $\vec{l}_{[100]}$, $\vec{l}_{[0\bar{1}1]}$, and $\vec{l}_{[\bar{1}\bar{1}1]}$. Bottom: triangular 2D island on crystal face; step edges parallel to intermolecular vectors, with step edge vectors $\vec{s}_{[100]}$, $\vec{s}_{[0\bar{1}1]}$, and $\vec{s}_{[\bar{1}\bar{1}1]}$.

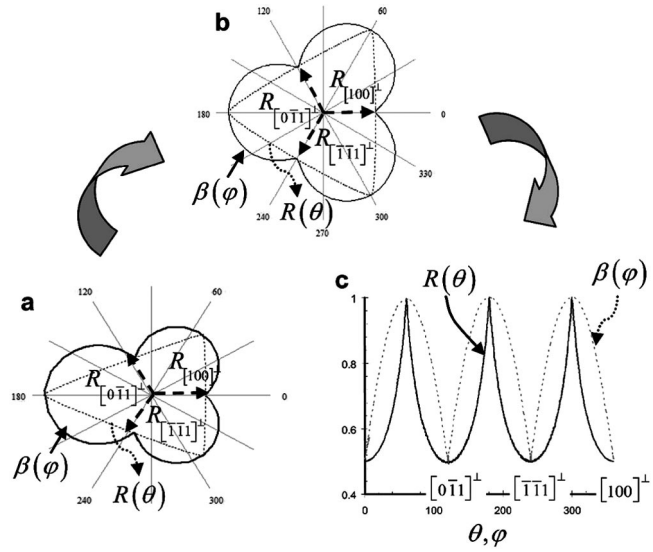


**Figure 6.** Inverse 2D-Wulff construction of the equilibrium island shape (EIS): (a) EIS and step formation energy per unit length $\beta$ in polar coordinates; (b) normalized EIS and $\beta$ in polar coordinates; (c) $\beta$-normalized EIS and $\beta$ in Cartesian coordinates.

difference in intermolecular distances, we normalize the EIS with $\vec{l}_{[100]}/\vec{l}_{[0\bar{1}1]}/\vec{l}_{[\bar{1}\bar{1}1]}$. Calculating the inverse 2D Wulff construction of the EIS, we identify three distinct directions $\vec{s}_{[100]^\perp}$, $\vec{s}_{[0\bar{1}1]^\perp}$, and $\vec{s}_{[\bar{1}\bar{1}1]^\perp}$ with a period of $2\pi/3$ for which $\beta$ reaches an equal minimum value (Figure 6a−c). Hence we have shown that, if we assume that the islands have equilibrium shapes, application of the 2D Wulff construction correctly predicts the measured ratio of island edge lengths.

On the basis of the equality of the step formation energy $\beta$ for the three step edge directions, we conclude that the amount and type of unsatisfied bonds per unit length for these three step edges are equal. Therefore, we can generalize our ensuing findings on tangential growth to all three directions. Consequently, conclusions made for one step direction will be applicable to the other remaining directions.

**3.2.2. Tangential Growth-Step Dynamics.** Growth parallel to the crystal surface (tangential growth) proceeds through the horizontal spreading of molecular layers across the crystal surface. This step advancement is the result of the incorporation of new growth units random into the step (1D nucleation) or in specific attachment sites, named kinks. Two types of mass transfer mechanisms procure the delivery of these growth units to the advancing step edges, namely the process of direct incorporation and the two-step process of surface diffusion followed by step incorporation. In the case of direct incorporation from solution, competition for the supply between contiguous steps is small. If the supply is, however, limited to the diffusion of molecules adhering to the surface (admolecules), competition will be substantial if the diffusion length of the adhered growth units is larger than the distance between two neighboring steps. This will result in a strong overlap of the surface diffusion fields of the growth steps and step interaction as a consequence. Ascertaining the relative importance of the two mass transport systems entails the visualization of either the surface species or the advancing growth steps. Because the surface diffusivity of TIM is unknown, we use the 2D diffusivity of canavalin ($\sim 1 \times 10^{-12}$ m$^2$/s)[14] to estimate the velocity of TIM admolecules, resulting in $\sim 1 \times 10^4$ nm/s[14]. During the in situ AFM experiments we sampled a surface distance of approximately 400 nm with a frequency of 2.54 Hz equaling a tip velocity of $\sim 1 \times 10^3$ nm/s. This is too slow to visualize the diffusing admolecules. Because an increase in scanning velocity would increase the tip–sample interaction forces and thus increase the possibility to damage the surface, we were limited to scan frequencies of 2.54 Hz.

Nonetheless, evidence for the prevailing incorporation mechanism can be sought in the study of step dynamics.[32] Step incorporation/detachment events operate on a time scale (∼seconds) that is 2 orders of magnitude smaller than a typical AFM image acquisition time span (∼200 s). This incompatibility of timescales can be remedied by disabling the slow scan axis direction, hereby scanning the same line perpendicular to the nominal direction of the step edge as a function of time (1D sampling) and diminishing the scanning time to ∼0.4 s. Moreover, this technique allows us to separate the influence of spatial fluctuations on step dynamics from temporal fluctuations.[33] An example of a step trace image obtained for the (011) face is shown in Figure 7a.

These dynamical step fluctuations can be the result of various transport phenomena. One is where mass transport occurs only along the step through a process called true line diffusion (Figure 8). Another is where step perturbations result from mass exchange of the step with the solid surface phase (2D surface diffusion) and the surrounding liquid phase (direct incorporation). We can identify the presence of line diffusion by analyzing the time correlation curve $F(\Delta t)$ of the spatial displacements of the step edge, defined by[34]

$$F(\Delta t) = \langle [x(t+\Delta t) - x(t)]^2 \rangle \qquad (2)$$

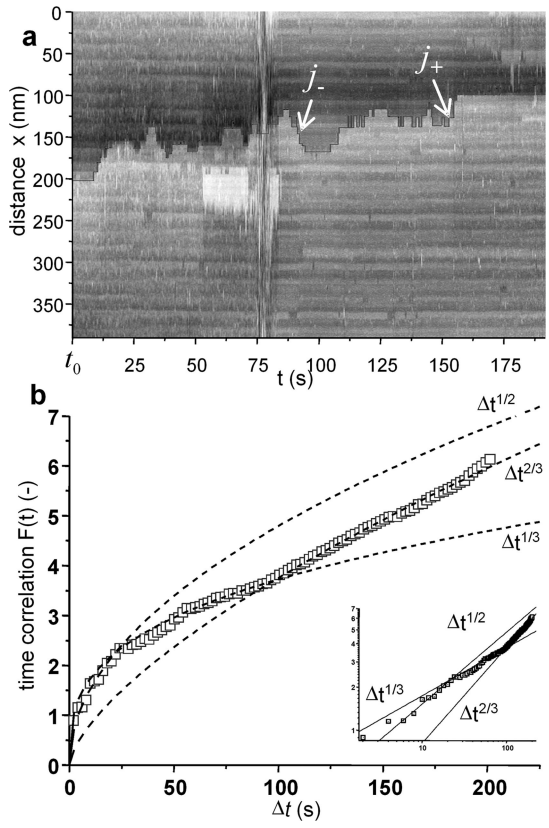


**Figure 7.** (a) Time evolution of the step position on the (011) face. A 1D-sampled image with the slow scan axis parallel to the step disabled at time $t = 0$ shows the molecular step displacement with detachment events ($j_-$) and attachment events ($j_+$); (b) Time correlation curve, characterizing mean square displacement of step location as a function of time $\Delta$t, corresponding the step trace shown in (a): solid squares indicate data, lines fit with exponential dependencies at ½ or ⅓ and ⅔ are shown with dashed lines. The goodness of fit is indicated by respective $R^2$ values of 0.953, 0.968, and 0.996. Inset: logarithmic plot of $F(t)$.

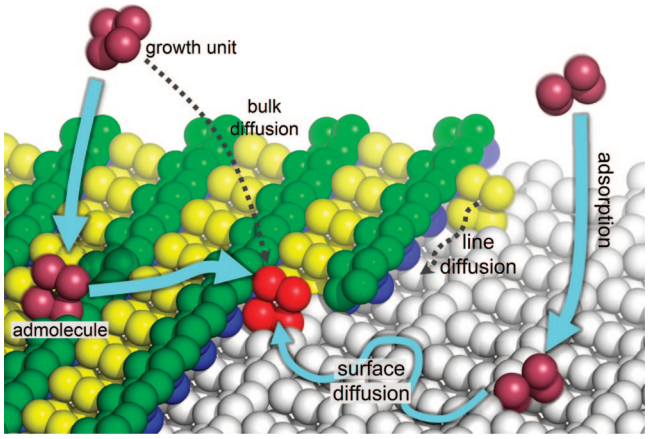


**Figure 8.** Two possible pathways for a growth unit from solution into a step: direct incorporation from solution; step integration as a result of surface diffusion. Reorganization of the step occurs through line diffusion.

with averaging over respective $\Delta t$, $x(t)$ the step location expressed as the ratio of the length of step trace increment to the linear dimension of a single TIM tetramer (7 nm), at time $t$ and $\Delta t$ time increments of 2 s. These results can be interpreted using equilibrium step dynamics models.[35,32] As is evident from Figure 7b, the obtained correlation curve displays two, possibly three, different time regimes. At smaller timescales, the correlation curve can be fitted using a power law with either exponent ½ or ⅓ and at larger timescales the exponent ⅔ is obtained. These power law curve fittings were performed using the nonlinear least-squares method from Origin 7.0. As pointed out by Ihle et al.,[32] the predicted sequence of exponents at intermediate and large time scales depends on the limiting transport mechanism and the presence of a weak or strong Schwoebel effect (i.e., different rates of incorporation of admolecules between the up-side and the down-side steps sites due to an energy barrier at the step edge). If supply is limited to diffusion, transport on the terrace or in the bulk solution is slow. Conversely, in the kinetically limited case slow attach/detachment events are the rate determining step. Yet, regardless of the limiting transport mechanism, step perturbations brought about by a mere conformational reorganization of the step through line diffusion are predicted to follow a power law ¼. The absence of a ¼-power law in the fitted data presented in Figure 7b indicates that line diffusion contributes at most only marginally to the temporal step fluctuations. This allows us to attribute the step trace displacement events to the exchange of growth units with the surrounding phases, i.e., the terrace and solution phase. Note that exponents ½ and ⅓ are predicted by equilibrium step dynamics;[32] however, we did not find any theories predicting the exponent ⅔ at larger timescales.

**3.2.3. Surface Diffusion.** Because line diffusion has a negligible influence on step dynamics, we can test the existing model of direct incorporation from solution by examining the net flux into the step given by[36,37]

$$j_+ - j_- = \nu_+ C_e \Omega \exp\left(-\frac{U_{\max}}{k_B T}\right)\left[\frac{C}{C_e} - 1\right], \nu_+ = \frac{D}{\Lambda a} \qquad (3)$$

and

$$\frac{j_+}{j_-} = \frac{C}{C_e} \qquad (4)$$

with $U_{\max}$ the energy barrier for incorporation into the kinks, $\Omega$ the crystal volume per molecule, $D$ the diffusion coefficient, $\Lambda$ the radius of curvature of the surface−molecule interaction potential around its maximum at $U_{\max}$, $k_B$ the Boltzmann constant, and $a$ a typical size of the attaching species in the lattice. For the time trace shown in Figure 7a during a measuring period of 192 s, there were in total 54 attachment and 45 detachment events, giving for the left part of eq 4 $j_+/j_- \leq 1.2$. This ratio is an upper estimate because any attachment/detachment events that occurred within the temporal resolution of ~0.4 s remain undetected. The growth velocity for the step edge displayed in Figure 7a is $\Delta x/\Delta t = 125.2$ nm/201 s = 6.2 Å/s.

At a used $C$ of 0.2 mg/mL TIM and a precipitant concentration of 2 M ammonium sulfate, $C_e$ is 0.043 mg/mL giving for the right part of eq 4 $C/C_e = 0.2/0.043 = 4.7$. The violation of eq 4 indicates that the model of direct incorporation from solution is not applicable in this case and shows that the mechanism of incorporation through surface diffusion is more plausible. This violation cannot be ascribed to solute depletion effects in the near vicinity of the surface, because this component would become considerable at ~10–100× higher growth rates.[38] If we assume Langmuir adsorption where the relative surface coverage $\theta = C(C + B)$ ($\theta = n_s/n_{s\infty}$ is the relative surface coverage, $B$ is the Langmuir constant), the following inequality for a nonsaturated state applies, $n_s/n_e \leq C/C_e$. When combined with the expression for the in- to outflux in case of surface diffusion $n_s/n_e = j_+/j_-$,[36,37] the former inequality yields $j_+/j_- \leq$

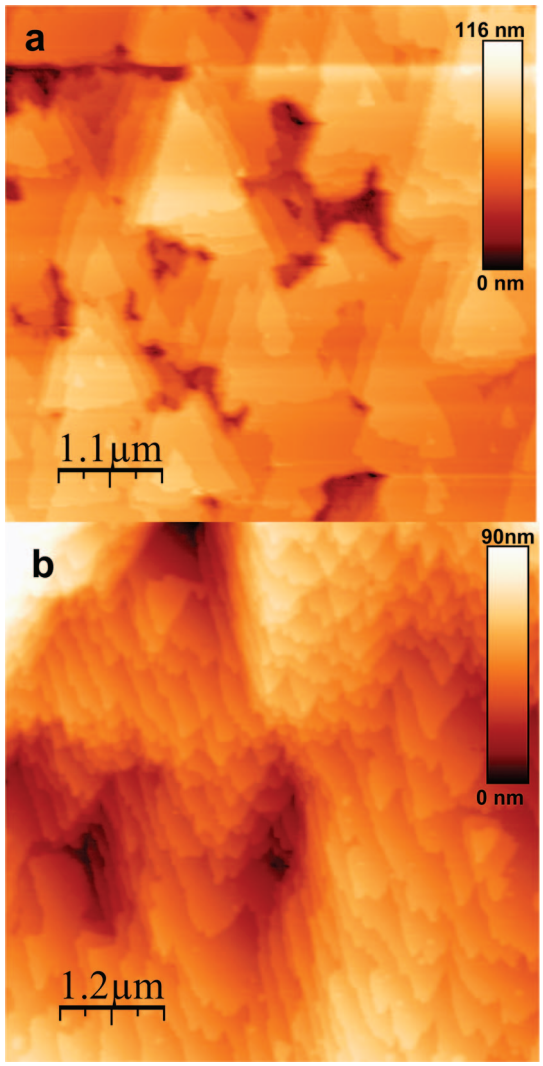


**Figure 9.** (a) 2D-nucleation resulting in the formation of multilayer stacked structures; (b) Step bunching resulting in macrosteps.

$C/C_e$. Therefore the mechanism of incorporation of admolecules corroborates our observed lower ratios of in- to outflux.

Using $j_+/j_- \leq 1.2$ and $C/C_e = 0.2/0.043$, we can now estimate $B$ to be 0.011 mg/mL. This gives (with $C = 0.2$ mg/mL) for the relative surface coverage $\theta \geq 0.95$. When deducing models for surface diffusion, an adsorption site is typically considered to correspond to a single lattice site. This would imply a surface coverage similar to 95% of a full crystal layer for this case. As pointed out by Chen et al. for the case of (apo)ferritin,[19] it seems unlikely that the packed admolecules would possess an adequate mobility for growth. Our results on TIM therefore also dispute the assumption that molecular adsorption sites match crystal lattice sites of a completed growth layer.

The conclusion of surface diffusion resulting from the violation of eq 4 is not contradicted by the presence of multilayer stacks of 2D islands with a central island that is much wider than the underlying terraces ("wedding-cake"-like structures)[39] observed on growing (011) faces (Figure 9a). These structures can be explained by the existence of an extra contribution[40–42] $E^{sch}$ to the energy barrier for admolecules incorporating into a step from the lower terrace.[43] The phenomenon of preferential incorporation of particles into steps from the upper terrace is called the inverse Schwoebel effect (ISE). Presence of the ISE can be indirect evidence of surface diffusion. Additionally, we observe the formation of large step trains on the (011) face resulting in step bunching as can be seen in Figure 9b. Although it has been shown that the morphological instability of step bunching may be caused by the ISE,[44,45] we cannot however rule out the possibility that 'kinematic waves of steps' initiated by impurity adsorption or solution flow[46,47] are the cause of macrostep existence for this case.

Although during the last two decades much debate has taken place on the relevance of surface diffusion in solution crystal growth,[9–13,16–18] evidence indicative of the importance of surface diffusion controlled kinetics in protein crystal growth has accumulated gradually in the literature.[14–17,19] How can this preferential incorporation of admolecules over molecules in the bulk be explained? One of the potential reasons is that biological macromolecules experience a high rotational entropic barrier for kink incorporation because of their size, geometrical complexity, and structural anisotropy.[48] Because no sufficient torque reorienting the biomolecule for correct incorporation is expected, the molecule approaches the kink at random orientation.[49] The probability that a molecule will arrive at a kink with an orientation that is relevant for regular attachment is estimated to be $1 \times 10^{-2}$ to $1 \times 10^{-3}$.[36] In addition to this configurational obstacle, macrobond patches between future neighbors (on the incoming molecule, the molecules belonging to the underlying layer and the molecules in the kink) should be dehydrated. As opposed to direct incorporation from solution where all these events need to operate in a concerted way and therefore result in a large activation barrier, surface diffusion is a two-step process where the barriers for adsorption and incorporation into the step are separated.[14] Quantitative data on ferritin adsorption and incorporation barriers ($U_{adsorption} \leq 26$ kJ/mol; $U_{step} \leq 44$ kJ/mol)[19] compared to the potential barrier for direct incorporation for ferritin ~88 kJ/mol strengthen this notion.

Despite the fact that it has been argued that two-dimensional surface diffusion has a high potential barrier,[5] estimated potential barriers of $U_{adsorption} \approx 26$ kJ/mol and $U_{step} \approx 9.6$ kJ/mol for the case of canavalin[14] hint at the possibility that adsorption to the surface directs the biomolecule into an orientation more optimal for incorporation.

**3.2.4. Growth Units.** The frequencies of attachment $j_+$ of building units to kinks and their detachment $j_-$ are elementary parameters of crystal growth and are used in almost all models of crystal growth. Experimental data on $j_+$ and $j_-$ for protein crystallization however is limited to the case of (apo)ferritin.[19,50,20] On the basis of the 1D-sampled images, we determined the one-dimensional size distribution of units attaching to and detaching from the [100] step edge (Figure 10). The 7 nm peak can be interpreted as the addition of a single tetramer when compared to the X-ray data shown in Figure 10a. Likewise, the small 15 nm peak can be correlated with the attachment/detachment event of a single unit cell. It is conceivable that the dominating peak at 11 nm stems from an intermediate kinetic state, i.e. a partial unit cell that is in the process of being completed and formed during the time dead zone of the experiment, i.e., the temporal resolution of 0.4 s. We found similar results for the kinetics of incorporation at the $[\bar{1}\bar{1}1]$ step (see the Additional Information).

What is the growth unit for the crystallization of TIM? Most likely the dominating growth unit is a single TIM tetramer. Although larger sized attachment/detachment events are observed, it is probable that they are formed on a time scale smaller than 0.4 s. Indeed, when looking at the kinetics of incorporation, more specifically the time intervals between individual attach-

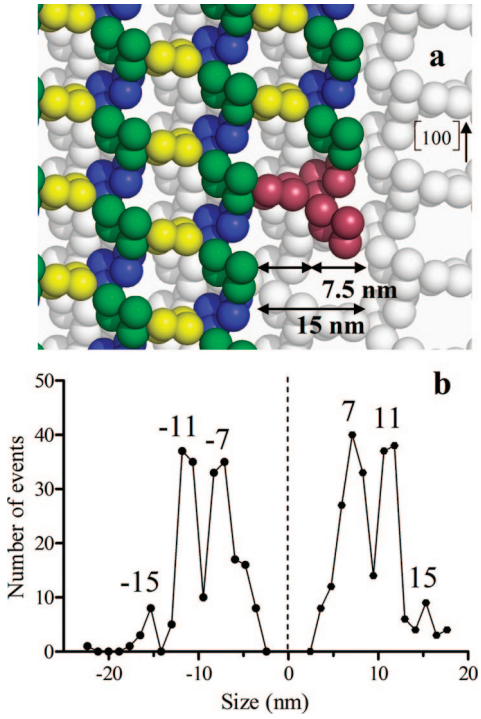


**Figure 10.** (a) [100] step edge on the (011) face. The unit cell comprising 3 tetramers is displayed in purple (single sphere represents a single monomer). (b) Size distribution of units arriving to (positive values) and detaching (negative values) from the [100] step.

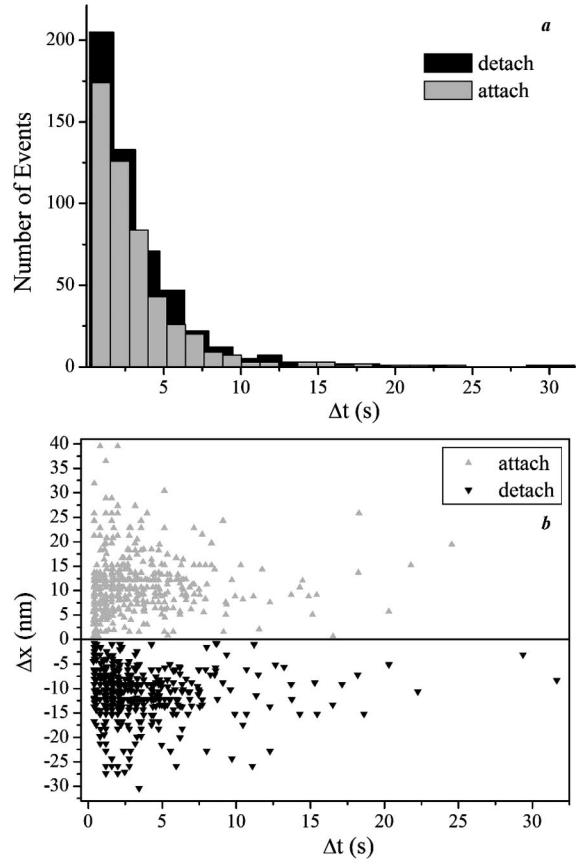


**Figure 11.** (a) Histogram of time intervals $\Delta t$ between individual attachment (light grey) and detachment events (dark grey), the data follows an exponential decay as a function of time. (b) Linear size of units attaching to (light grey) or detaching from (dark grey) the step as a function of the time interval $\Delta t$ between two successive events.

ment and detachment events, we find an exponential decay as a function of time. From this data, we conclude that the time interval between a large part of the events is of the order of <1 s (Figure 11).

Clearly, the kinetics of the system operate on a time scale equal to or smaller than the temporal resolution obtained in our experimental setup. This is exemplified by the absence of a clear maximum in the time distribution of attachment events (Figure 11a). Such a maximum would be expected because molecules incorporate at finite velocities in the step. This suggests that the addition of units with linear dimensions larger than a single TIM tetramer, can be the result of a series of incorporation events within the time frame of 0.4 s. Also, we found no correlation between the linear size of units attaching to or detaching from the step and the time interval between two successive events (Figure 11b).

## 4. Conclusion

To summarize, in this article, we have presented for the first time high-resolution atomic force data on the crystallization of TIM. We have shown that normal growth on the (011) crystal face of triosephosphate isomerase is dominated by two-dimensional nucleation in the tested supersaturation range from 1.6 to 5.8. From the normalized equilibrium island shape of the anisotropic 2D islands, it was determined that the three step edges have an equal step edge free energy. On the basis of step edge dynamics and mesoscale data, we conclude that surface diffusion contributes significantly to surface kinetics of the (011) face. Hence, the ruling pathway of a growth unit from the bulk solution to a kink is surface adsorption followed by two-dimensional surface diffusion.

For this system, we determined the frequencies of attachment and detachment of building blocks from steps. On the basis of the size-distribution of incorporation events, a single TIM tetramer is identified as a growth unit.

**Acknowledgment.** We thank P. Vekilov for helpful critical discussions; L. Buts for aiding with the in silico modeling of the Miller planes; W. Keegstra (University of Groningen, The Netherlands) for providing the Grip software and T. Ihle for critical remarks. This work was supported by the Flanders Interuniversity Institute for Biotechnology (VIB), the Research Council of the VUB, and the Belgian Federal Science Policy Office (DWTC). We thank the European Space Agency for financing in the context of Prodex project C90035 and AO004.

**Supporting Information Available:** Two additional figures (PDF). This material is available free of charge via the Internet at http://pubs.acs.org.

## References

(1) Berman, H. M.; Bhat, T. N.; Bourne, P. E.; Feng, Z.; Gilliland, G.; Weissig, H.; Westbrook, J. *Nat. Struct. Biol.* **2000**, *7*, 957–959.
(2) Burton, W. K.; Cabrera, N.; Frank, F. C. *Philos. Trans. R. Soc. London* **1951**, *243*, 299–358.
(3) Vekilov, P. G.; Alexander, J. I. D. *Chem. Rev.* **2000**, *100*, 2061–2089.
(4) Vekilov, P. G. In *Methods in Molecular Biology, Vol. 300: Protein Nanotechnology, Protocols, Instrumentation and Appliciations*; Vo-Dinh, T., Ed.; Humana Press: Totowa, NJ, 2005; p 15.
(5) Chernov, A. A. *J. Mater. Sci.: Mater. Electron.* **2001**, *12*, 437–449.
(6) Gratz, A. J.; Hillner, P. E.; Hansma, P. K. *Geochim. Cosmochim. Acta* **1993**, *57*, 491–495.

(7) Bostanov, V.; Staikov, G.; Roe, D. K. *J. Electrochem. Soc.* **1975**, *122*, 1301–1305.
(8) Rodriguez-Hornedo, N.; Wu, H. J. *Pharm. Res.* **1991**, *8*, 643–648.
(9) Chernov, A. A. *Prog. Cryst. Growth Chem.* **1993**, *26*, 121–151.
(10) Chernov, A. A. *Contemp. Phys.* **1989**, *30*, 251–276.
(11) Vekilov, P. G.; Kuznetsov, Y.; Chernov, A. A. *J. Cryst. Growth* **1992**, *121*, 643–655.
(12) De Yoreo, J. J.; Land, T. A.; Dair, B. *Phys. Rev. Lett.* **1994**, *73*, 838–841.
(13) Land, T. A.; De Yoreo, J. J.; Lee, J. D.; Ferguson, J. R. In *Evolution of Thin Film and Surface Structure and Morphology*; Demczyk, B. G., Ed.; Materials Research Society: Warrendale, PA, 1995; p 45.
(14) Land, T. A.; De Yoreo, J. J.; Lee, J. D. *Surf. Sci.* **1997**, *384*, 136–155.
(15) Reviakine, I. *J. Am. Chem. Soc.* **2003**, *125*, 11684–11693.
(16) Vekilov, P. G.; Monaco, L. A.; Rosenberger, F. *J. Cryst. Growth* **1995**, *156*, 267–278.
(17) Vekilov, P. G.; Thomas, B. R.; Rosenberger, F. *J. Phys. Chem. B* **1998**, *102*, 5208–5216.
(18) Chernov, A. A.; Rashkovich, L. N.; Yaminski, I. V.; Gvozdev, N. V. *J. Phys.: Condens. Matter* **1999**, *11*, 9969–9984.
(19) Chen, K.; Vekilov, P. G. *Phys. Rev. E* **2002**, *66*, 21606–1–21606–5.
(20) Petsev, D. N.; Chen, K.; Gliko, O.; Vekilov, P. G. *Proc. Natl. Acad. Sci. U.S.A.* **2003**, *100*, 792–796.
(21) Maes, D.; Zeelen, J. P.; Thanki, N.; Beaucamp, N.; Alvarez, M.; Thi, M. H.; Backmann, J.; Martial, J. A.; Wyns, L.; Jaenicke, R.; Wierenga, R. K. *Proteins* **1999**, *37*, 441–453.
(22) Gilliland, G. L.; Tung, M.; Blakeslee, D. M.; Ladner, J. E. *Acta Crystallogr., Sect. D* **1994**, *50*, 408–413.
(23) Khare, S. V.; Kodambaka, S.; Johnson, D. D.; Petrov, I.; Greene, J. E. *Surf. Sci.* **2003**, *522*, 75–83.
(24) Malkin, A. J.; Kuznetsov, Y. G.; McPherson, A. *J. Cryst. Growth* **1999**, *196*, 471–488.
(25) Malkin, A. J.; Kuznetsov, Y. G.; Glantz, W.; McPherson, A. *J. Phys. Chem.* **1996**, *100*, 11736–11743.
(26) Kuznetsov, Y. G. *J. Cryst. Growth* **1996**, *168*, 63–73.
(27) Yau, S. T.; Vekilov, P. G. *Nature* **2000**, *406*, 494–497.
(28) McPherson, A. In *Crystallization of Biological Macromolecules*; Bianco, C., Ed.; Cold Spring Harbor Laboratory Press: New York, 1999.
(29) Gunther, S.; Kopatzki, E.; Bartelt, M. C.; Evans, J. W.; Behm, R. J. *Phys. Rev. Lett.* **1994**, *73*, 553–556.
(30) Kodambaka, S.; Khare, S. V.; Petrov, I.; Greene, J. E. *Surf. Sci. Rep.* **2006**, *60*, 55–77.
(31) Kodambaka, S.; Khare, S. V.; Petrova, V.; Vailiones, A.; Petrov, I.; Greene, J. E. *Vacuum* **2004**, *74*, 345–351.
(32) Ihle, T.; Misbah, C.; Pierre-Louis, O. *Phys. Rev. B* **1998**, *58*, 2289–2309.
(33) Giesen-Seibert, M.; Jentjens, R.; Poensgen, M.; Ibach, H. *Phys. Rev. Lett.* **1993**, *71*, 3521–3524.
(34) Bartelt, N. C.; Goldberg, J. L.; Einstein, T. L.; Williams, E. D. *Surf. Sci.* **1992**, *273*, 252–260.
(35) Williams, D.; Bartelt, M. C. *Science* **1991**, *251*, 393–400.
(36) Chernov, A. A.; Komatsu, H. In *Science and Technology of Crystal Growth*; van der Eerden, J. P., Bruinsma, O. S. L., Eds.; Kluwer Academic: Dordrecht, The Netherlands, 1995; pp 67.
(37) Chernov, A. A.; Komatsu, H. In *Science and Technology of Crystal Growth*; van der Eerden, J. P., Bruinsma, O. S. L., Eds.; Kluwer Academic: Dordrecht, The Netherlands, 1995, pp 329.
(38) Lin, H.; Petsev, D. N.; Yau, S. T.; Thomas, B. R.; Vekilov, P. G. *Cryst. Growth Des.* **2001**, 73–79.
(39) Stäuble-Pümpin, B.; Mendoza, G. A.; Prieto, P.; Dam, B. *Supercond. Sci. Technol.* **2002**, *15*, 296–301.
(40) Ehrlich, G.; Hudda, F. G. *J. Chem. Phys.* **1966**, *44*, 1039–1049.
(41) Schwoebel, R. L.; Shipsey, E. J. *J. Appl. Phys.* **1966**, *37*, 3682–3686.
(42) Pierre-Louis, O.; D'Orsogna, M. R.; Einstein, T. L. *Phys. Rev. Lett.* **1999**, *82*, 3661–3664.
(43) Dumont, H.; Monteil, Y.; Bouix, J. *Appl. Surf. Sci.* **2000**, *161*, 286–290.
(44) Schwoebel, R. L. *J. Appl. Phys.* **1969**, *40*, 614–618.
(45) Sato, M.; Uwaha, M. *Phys. Rev. B* **1995**, *51*, 11172–11175.
(46) Chernov, A. A. In *Modern Crystallography III. Crystal Growth*; Springer-Verlag: Berlin, 1984.
(47) Booth, N. A.; Chernov, A. A.; Vekilov, P. G. *Phys. Rev. E* **2004**, *69*, 011604–011610.
(48) Chernov, A. A. *Acta Crystallogr., Sect. A* **1998**, *54*, 859–872.
(49) Chernov, A. A. *J. Struct. Biol.* **2003**, *142*, 3–21.
(50) Yau, S. T.; Thomas, B. R.; Vekilov, P. G. *Phys. Rev. Lett.* **2000**, *85*, 353–356.

CG0703691